PCCP

ARTICLE TYPE

Cite this: DOI: 00.0000/xxxxxxxxxx

Lipid bilayers as potential ice nucleating agents†

Christopher M. Miles,[a] Pin-Chia Hsu,[b] Ann M. Dixon,[a] Syma Khalid,[bc] and Gabriele C. Sosso*[a]

Received Date
Accepted Date

DOI: 00.0000/xxxxxxxxxx

Cellular damage is a key issue in the context of cryopreservation. Much of this damage is believed to be caused by extracellular ice formation at temperatures well above the homogeneous freezing point of pure water. Hence the question: what initiates ice nucleation during cryopreservation? In this paper, we assess whether cellular membranes could be responsible for facilitating the ice nucleation process, and what characteristics would make them good or bad ice nucleating agents. By means of molecular dynamics simulations, we investigate a number of phospholipids and lipopolysaccharide bilayers at the interface with supercooled liquid water. While these systems certainly appear to act as ice nucleating agents, it is likely that other impurities might also play a role in initiating extracellular ice nucleation. Furthermore, we elucidate the factors which affect a bilayer's ability to act as an ice nucleating agent; these are complex, with specific reference to both chemical and structural factors. These findings represent a first attempt to pinpoint the origin of extracellular ice nucleation, with important implications for the cryopreservation process.

1 Introduction

Cryopreservation is key to delivering the next generation of medical treatments, such as regenerative and translational medicine.[3–5] The aim is to store biological material via freezing[6], which unfortunately results in some extent of cellular damage[7–9]. Particularly when opting for the slow-freezing approach, it is essential to control the formation of ice.[10,11] Several so-called cryoprotectants[12–14] have been identified to limit the growth rate of the ice phase. However, to date we have little ability to affect the ice nucleation process itself.

Almost invariably, extracellular ice formation during cryopreservation takes place at mild supercooling, that is at temperatures far higher than the onset of homogeneous nucleation for pure water. This is indicative of the fact that ice nucleation must occur heterogeneously, but which entities are responsible for this process are yet to be determined. The extracellular, aqueous medium contains a number of impurities. However, it is possible that the cellular membrane itself can act as an ice nucleating agent. In fact, previous studies[1,15,16] suggest that certain components of cellular membranes, such as cholesterol (CHL, see figure 1(c)), are excellent ice-nucleating agents, albeit the extent to which phospholipids (which constitute the majority of the cellular membrane) can facilitate the formation of ice remains an open question.

In this work, we investigate the potential of a diverse portfolio of lipid bilayers — the building blocks of cellular membranes — as ice nucleating agents. In particular, we systematically assess the emergence of pre-critical ice nuclei at the interface between lipid bilayers and supercooled water across systems containing increasing amounts of cholesterol. We also consider lipids that possess a net charge, so as to probe the effects of local electric fields on the nucleation process. 1,2-Dipalmitoyl-*sn*-glycero-3-phosphocholine (DPPC, see figure 1(a)) bilayers are prototypical models of cellular membranes; having been the subject of many studies[17–19], both computational and experimental in nature. It's worth noting also that phosphatidylcholines (such as DPPC) are common constituents of cellular membranes.[20] Thus, DPPC is an excellent candidate to further our understanding of ice formation in biological matter. 1,2-Dimyristoyl-*sn*-glycero-3-phosphatidylinositol (DMPI, see figure 1(b)) is another phospholipid with a different headgroup to DPPC, notably with a negative overall charge.

Additionally, we take into account asymmetric phospholipid-lipopolysaccharide (LPS) membranes, coated (or otherwise) with sugars. These LPS systems are representative of the outer membrane of Gram-negative bacteria[21,22] and are intended to probe a complex biological system closer to actual cellular membranes (which all exhibit a coating rich in sugar-based molecules, termed

[a] *Department of Chemistry, University of Warwick, Coventry, CV4 7AL, United Kingdom. E-mail: g.sosso@warwick.ac.uk*
[b] *School of Chemistry, University of Southampton, Southampton, SO17 1BJ, United Kingdom*
[c] *Department of Biochemistry, University of Oxford, Oxford, OX1 3QU, United Kingdom.*

† Electronic Supplementary Information (ESI) available: comparing water layer to theoretical orientational order parameter (θ) values for homogeneous water; system-by-system size distribution of largest icy clusters per frame; filtering icy clusters by minimum size of 30 or 40 molecules; comparing pure CHL bilayer to previous work on CHL crystals[1] and monolayers[2]; RaLPS sugar distribution. See DOI: 10.1039/cXCP00000x/

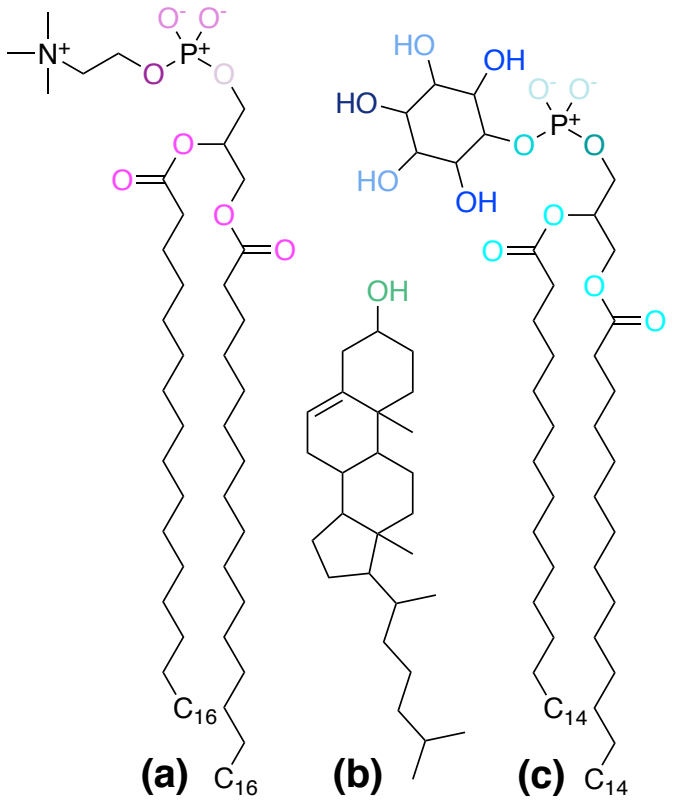

Fig. 1 The chemical structures of (a) DPPC (b) CHL and (c) DMPI. The hydrogen bonding sites are coloured according to the palette reported in figure 9.

the glycocalyx or pericellular matrix)[23], as well as assessing the effect of sugars on ice nucleation. Specifically, we look at three membranes: one with a purely lipid A leaflet; the "deep rough mutant" ReLPS, with two 3-deoxy-D-manno-octulosonic acid (Kdo) units linked to each lipid A molecule; and RaLPS, with the complete oligosaccharide core.[24,25]

We find that all the bilayers we have studied promote ice nucleation to some extent, and that both the bilayer topology and chemistry (particularly in terms of their ability to form hydrogen bonds with water molecules) have an impact on the efficacy of the bilayer as an ice nucleating agent. Introducing CHL into DPPC bilayers leads to a substantial increase in the structural ordering (and thus, the ice nucleating potential) of these systems, although at naturally occurring concentrations ($< 50\,\text{mol}\%$)[20,26] it is not clear whether the CHL improves or lessens the ice nucleating effect. Despite an increase in hydrogen bonding sites, DMPI does not appear to act as a significantly better ice nucleating agent than DPPC. Finally, it appears that sugar-coated LPS can also facilitate the formation of ice at the bilayer-water interface.

In contrast with previous work on CHL monolayers[2], we find that more ordered bilayers often are less efficient at nucleating ice than less well ordered bilayers when there are multiple different lipid constituents. We explain this apparent contradiction by the reduced number and accessibility of hydrogen bonding sites in these mixed bilayers. In particular, CHL embeds deeply into DPPC bilayers, leaving its very active hydroxyl group mostly inaccessible.

By comparing the propensity for pre-critical ice nuclei to form in the proximity of the bilayer with what we have previously observed for CHL crystals[1] (which are excellent ice nucleating agents, active at only a few degrees below $0\,^{\circ}\text{C}$)[27], we can estimate the potency of these systems relative to that of other biological ice nucleators. While lipid bilayers do display some potential, we conclude that cellular membranes alone cannot be the sole ice nucleating agents responsible for the extracellular ice formation observed in the context of cryopreservation. Thus, we hope that our findings will make a contribution to the ongoing quest towards the identification of what drives ice nucleation at the mild supercooling, which characterises the emergence of extracellular ice formation during slow-freezing protocols.

2 Methods

2.1 Simulation details

2.1.1 DPPC-CHL/DMPI Systems.

Eleven DPPC-CHL/DMPI lipid bilayer systems were constructed, using CHARMM-GUI[28–32], with 30 lipids per leaflet (60 per system). The number of each lipid per system, together with the in-plane dimensions of the simulation box, after equilibration and quenching, are listed in table 1. The systems have square cross sections so the x and y dimensions are the same. A water layer 30 Å thick was placed either side of the bilayers, using the molecular dynamics package GROMACS[33–39] (see figure 2).

Molecular dynamics (MD) simulations were used to probe the emergence of pre-critical ice nucleation. The force-field used to model the lipids was CHARMM36[40–45] and the TIP4P/Ice[46] force field was used for the water molecules — this combination of force fields has been shown to accurately reproduce the properties of supercooled liquid water and ice in recent studies[47,48]. Three dimensional periodic boundary conditions were used. An initial energy minimisation was carried out, using the SETTLE[49] algorithm to constrain the geometry of the water molecules, and the LINCS[50] algorithm to constrain the bilayer geometry. Subsequently, a number of initial equilibration runs were carried out at 323.15 K, sampling the NVT ensemble, with three-dimensional periodic boundary conditions. The fairly high temperature of 323.15 K was chosen to avoid the gel phase transition for DPPC, which occurs at around 305–315 K.[51]

System name	Number of lipids per leaflet DPPC	CHL	DMPI	Box x [nm]
Pure DPPC	30	-	-	3.56
20 mol% *CHL*	24	6	-	3.56
40 mol% *CHL*	18	12	-	3.37
60 mol% *CHL*	12	18	-	3.37
80 mol% *CHL*	6	24	-	3.35
Pure CHL	-	30	-	3.31
20 mol% *DMPI*	24	-	6	3.91
40 mol% *DMPI*	18	-	12	4.04
60 mol% *DMPI*	12	-	18	4.05
80 mol% *DMPI*	6	-	24	4.20
Pure DMPI	-	-	30	4.12

Table 1 Lipid composition of DPPC-CHL/DMPI systems simulated and in-plane dimensions after equilibration and quenching

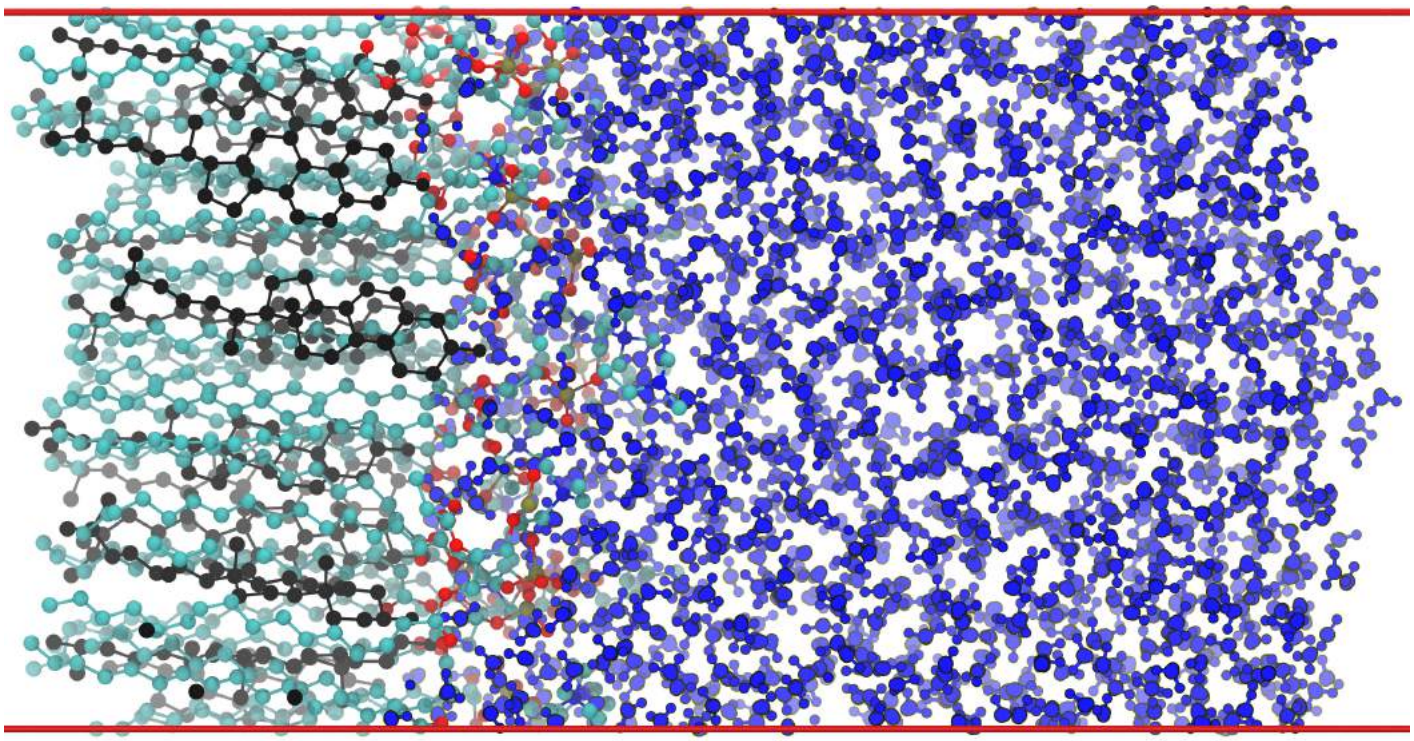

Fig. 2 Representative snapshot of (half of) a DPPC-CHL/water system, 40 mol% CHL (coloured in black). Water molecules are coloured in blue. Within the DPPC molecules, carbon, oxygen, phosphorus and nitrogen atoms are coloured in cyan, red, yellow and blue, respectively. Hydrogen atoms belonging to DPPC or CHL molecules are not shown. The water layer is in contact with an extended region of vacuum (see text).

Following these MD runs, the simulation box was elongated in the z-direction up to 270 Å, adding a vacuum region* on either side, in order to avoid artefacts caused by the slab geometry of the system[52]. An equilibration run of 20 ns, sampling the NVT ensemble at 323.15 K, was then carried out. Following the NVT run, a longer NpT run, of 200 ns, was carried out in order to equilibrate the system. Lipid bilayers on their own are capable of expanding and contracting by a reasonably large factor under pressure. A constant surface tension $\gamma_s = 120\,\mathrm{mJ\,m^{-2}}$ was imposed. This value of γ_s is consistent with literature[53] results: the surface tension of TIP4P/Ice water ($29.8\,\mathrm{mJ\,m^{-2}}$) multiplied by the number of interfaces (4), assuming that the value of γ_s is similar for water-vacuum interfaces and water-bilayer interfaces.

Following equilibration, the systems were quenched from 323.15 K to 233.15 K at a rate of $2.25\,\mathrm{K\,ns^{-1}}$, under constant (ambient) pressure and imposed surface tension ($120\,\mathrm{mJ\,m^{-2}}$). The systems were subsequently equilibrated at 233.15 K, using a 20 ns run under the NpT ensemble with surface tension of $120\,\mathrm{mJ\,m^{-2}}$. Once equilibrated at 233.15 K, extended MD runs of 70 ns–3.8 μs, depending on system, under the NVT ensemble were started. The DPPC-CHL systems were all run for at least 3 μs, however this was deemed unnecessary for the subsequent DPPC-DMPI and LPS systems.

* Figure 2 does not display these vacuum regions.

2.1.2 Lipopolysaccharide Systems.

Three asymmetric phospholipid-lipopolysaccharide (LPS) systems were simulated. These are representative of the outer membrane of Gram-negative bacteria.[21,22] The three systems consisted of a phospholipid leaflet and a lipid A leaflet, with varying amounts of sugars: 3-deoxy-D-manno-octulosonic acid (Kdo), L-glycero-D-manno-heptose (Hep), D-glucose (Glc) and D-galactose (Gal); coating the lipid A, distribution of these sugars is illustrated in the ESI†. The phospholipid leaflets consist of 1-palmitoyl-2-oleoyl-*sn*-glycero-3-phosphoethanolamine (POPE), 1-palmitoyl-2-oleoyl-*sn*-glycero-3-phosphoglycerol (POPG) and 1,10-palmitoyl-2,20-vacenoyl cardiolipin (PVCL2) for the Lipid A and ReLPS systems and 1-palmitoyl-2-vacenoyl-*sn*-glycero-3-phosphoethanolamine (PVPE), 1-palmitoyl-2-vacenoyl-*sn*-glycero-3-phosphoglycerol (PVPG) and PVCL2 for the RaLPS system. The exact composition and in-plane dimensions, after equilibration and quenching, of these bilayers can be found in table 2. Again, the box x and y dimensions are equal. The protocol discussed in the previous section for DPPC-CHL/DMPI bilayers has been adopted for the LPS systems. Note that "lipid A" is used to refer to both the system with no sugars (Lipid A) as well as the lipid molecule itself; in an attempt to prevent confusion, when the Lipid A system is meant, the L is capitalised.

2.2 Bond order parameters

In order to identify the ice nuclei, we have adopted the Steinhardt local bond order parameters[54]. These work via an averaging of the spherical harmonics of a chosen order, over the molecules

System	Lipid A	ReLPS	RaLPS
POPE[a]	145	145	90
POPG[a]	8	8	5
PVCL2	8	8	5
Lipid A	53	53	35
Kdo	0	106	70
Hep	0	0	140
Glc	0	0	105
Gal	0	0	35
Box x [nm]	9.14	9.48	7.94

[a]PVPE/PVPG for RaLPS

Table 2 Composition of LPS systems simulated (Number of molecules) and in-plane dimensions after equilibration and quenching

within the first coordination shell. Commonly the order chosen is 3, 4 or 6 for identifying cubic and hexagonal crystal structure. The Steinhardt parameter, of order l, for a molecule i, is defined as follows:

$$q_l(i) = \sqrt{\frac{4\pi}{2l+1}\sum_{m=-l}^{l}|q_l^m(i)|^2} \quad (1)$$

with the complex sub-parameters $q_l^m(i)$ defined thus:

$$q_l^m(i) = \langle Y_l^m(\mathbf{r_{ij}})\rangle_{j\in\mathbf{1}_i}$$

where $\langle\cdot\rangle_{i\in\mathbf{1}_i}$ denotes an ensemble average over the first coordination shell, *excluding i itself*, $\mathbf{r_{ij}}$ is the vector from molecule i to molecule j and Y_l^m indicate the spherical harmonics.

2.3 Largest icy cluster per frame

The largest "icy cluster" per frame was computed using the PLUMED2 software.[55–57] These clusters were computed as follows:

1. Filter all water molecules by q_6 (see equation (1)).
2. Compute contact matrix between molecules left after filtering.
3. Determine which cluster is the largest.

Note that for the DPPC-CHL and DPPC-DMPI systems, the two water layers are treated as one so it is truly the largest cluster per frame; for the LPS systems, which are asymmetric, the two water layers are treated separately, so we have two largest clusters per frame, one from each side.

2.4 Bilayer ordering

2.4.1 SMAC collective variable.

The degree of order within the bilayers can be assessed in multiple ways. The single molecule angle criteria (SMAC) is a collective variable which measures orientational order with respect to a defined molecular axis.[58] In our case, we define SMAC so that it is high, approaching 1, for systems where lipid tails are close to parallel; and lower for systems where lipids are more chaotically oriented. To define the SMAC parameter s_i, for a particular lipid molecule i, first we must define a molecular axis. In the case of our simulations, the axis is chosen to follow the (first) tail of each lipid in the bilayer with the exception of lipid A, where we use each of the four primary chains and PVCL2, where we use both of the primary chains.

We define a switching function f, which acts on the distance $\mathbf{r_{ij}}$ between two lipids i and j:

$$f(\mathbf{r_{ij}}) = \frac{1}{1+(2\mathbf{r_{ij}})^6},$$

and set $n_i = \Sigma_{i\neq j} f(\mathbf{r_{ij}})$. Now we define another switching function ψ, this time acting on the size of the coordination shell:

$$\psi(n_i) = \exp\left(-\frac{n_i}{6}\right).$$

Finally we define a Gaussian kernel function K, acting on the torsional angle θ_{ij} defined between the molecular axes of two lipids i and j:

$$K(\theta_{ij}) = \exp\left(-\frac{\theta_{ij}^2}{2\sigma^2}\right),$$

where σ is the width of the Gaussian; here we used $\sigma = 0.58$. Now we are ready to define the SMAC parameter:

$$s_i = \frac{(1-\psi(n_i))\,\Sigma_{i\neq j} f(\mathbf{r_{ij}})K(\theta_{ij})}{n_i}.$$

The SMAC parameter was computed using the SMAC collective variable from the PLUMED2 software.[55–57] This collective variable has typically been used in the past for nucleation studies rather than for membrane ordering.[59]

2.4.2 Voronoi area per lipid.

A second measure for the spatial ordering of bilayers is to compare the average surface area per lipid. This is achieved by computing the accessible area for each lipid via the construction of a Voronoi tessellation.[60,61]. In the case of CHL, the lone oxygen is used as the vertex, whereas for DPPC and DMPI the central glycerol carbon and the first carbon in each tail are used as vertices; this is to account for the difference in size between cholesterol and the phospholipids. These accessible areas were not computed for the LPS systems, as the leaflet we are interested in (lipid A with or without sugars) is homogeneous in-plane. For these systems, the average area per lipid A is computed by dividing the total surface area by the number of lipid A molecules. The accessible areas were computed using the built in area per lipid function of the FATSLiM package.[62] This method for calculating surface areas per lipid has been used extensively in previous membrane simulation studies.[19,60,61,63]

2.5 Water orientation

The orientational order parameter, θ, for a given water molecule, corresponds to the angle defined between the dipole moment (acting from positive to negative charge density) and the bilayer normal. An angle of $\theta = 0°$ indicates that the dipole moment is pointing perpendicularly away from the bilayer, while an angle of $\theta = 180°$ indicates where the dipole moment points toward the bilayer (see figure 3).

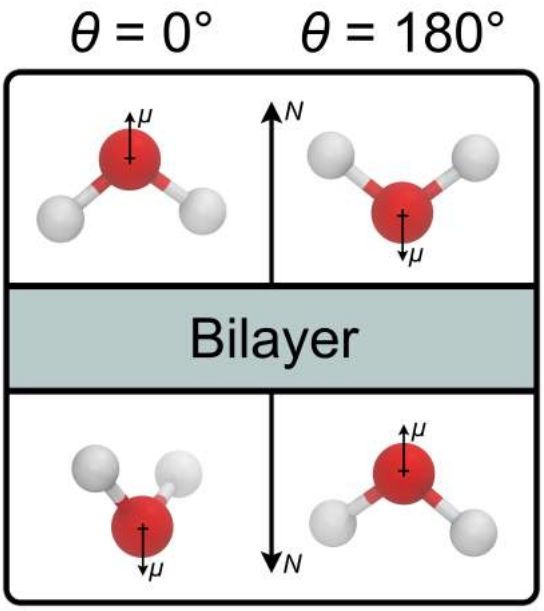

Fig. 3 Visual schematic of water dipole orientation at $\theta = 0°$ and $\theta = 180°$. The dipole moment (μ) for each water molecule and the bilayer normal (N) on either side are displayed.

3 Results and discussion

3.1 Ice nuclei at the lipid-water interface

Investigating heterogeneous ice nucleation by means of atomistic simulation is a very challenging as well as computationally expensive task.[64–68] However, we have demonstrated in previous studies[1,2,69,70] that quantifying the tendency for the pre-critical ice nuclei to occur at the interface with a given material (compared to the probability of occurring elsewhere within the water layer) provides an indication of a given surface ice nucleating ability.

Figures 4 to 6 show the distribution of largest pre-critical ice nuclei (see section 2.3) for the DPPC-CHL, DPPC-DMPI and LPS systems. For these graphs, we include only those clusters which contain at least 30 water molecules. The effect on the distribution of filtering by minimum sizes of 30 and 40 clusters is shown in the ESI.† A minimum of 30 was chosen as this avoids including the effect wherein small clusters form at the vacuum interface preferentially compared to in the bulk. A minimum of 40 was considered too strict as only around 6.5 % of frames in the DPPC-CHL/DMPI systems contained such a cluster. In comparison, around 30 % of frames in these systems contained a cluster of 30 or more molecules. Due to being considerably larger in-plane, the corresponding percentages of frames are much higher for the LPS systems.

We start our discussion with the DPPC-CHL systems (figure 4). Firstly, we notice that all of these bilayers, independent of the composition, facilitate the formation of ice nuclei at their interface with water. Interestingly, DPPC alone shows a similar ice nucleating potential to pure CHL, despite the fact that the DPPC-water interface is much more diffuse than the CHL-water one — that is to say the hydration layer for DPPC extends to a much greater extent. In previous work, we have provided experimental evidence of the activity of CHL monolayers as a function of surface coverage.[2] These systems display ice nucleating activity below $-15\,°C$, whilst crystalline CHL can nucleate ice at much warmer temperatures ($\sim -5\,°C$). As such, we believe that DPPC bilayers would display a weak ice nucleating activity, compared to potent biological ice nucleating agents such as CHL crystals,[1] Pseudomonas syringae[71,72] or pollen[73–76]. As we increase the content of CHL within the bilayer, the probability density at the bilayer-water interface decreases, reaching a minimum for the 40 mol% CHL composition, and then rises again until we reach pure CHL. As we shall discuss in greater detail in the next sections, this is due to both the structural order of the bilayers as well as the interplay between the hydrogen bonding sites provided by both DPPC and CHL. A comparison between the pure CHL bilayer, CHL crystals[1] and CHL monolayers[2] can be found in the ESI†, such bilayers appear to have similar, if not greater, ice nucleating potential than monolayers, but are much less active than crystalline CHL.

Similar trends are observed in the case of the DPPC-DMPI systems (figure 5). In fact, pure DMPI appears to be even more active than pure CHL, with a very pronounced peak of the probability density for the ice nuclei at the bilayer-water interface. In addition, the decrease of said peak as we progressively increase the DMPI fraction of the bilayer is less pronounced in comparison to the analogous trend in DPPC-CHL. Aside from the greater potential of DMPI to form hydrogen bonds with water, we will see in the next sections that the degree of order within DPPC-DMPI bilayers follows a different trend with respect to DPPC-CHL.

Finally, we consider the sugar-coated lipids, which offer a closer representation of the outer layer of the cellular membrane. These are asymmetric systems: as illustrated in figure 6, the "left" side of the bilayer features a phospholipid-water interface, whilst the "right" side of the bilayer presents lipid A (either sugar-coated or not). Focusing first on the phospholipid leaflet alone (left side), we observe a limited (certainly less pronounced than what we have observed for the majority of DPPC-CHL/DMPI systems) increase of the probability density for the ice nuclei to form within the interfacial region. Moving onto the right side of the membrane, it appears that Lipid A alone (top panel of figure 6) has little, if any, ice nucleating potential, as the probability for the icy clusters to form at the lipid-water interface is basically identical to that which we observe within the bulk of the water layer. However, the situation changes when introducing the sugars - see the ReLPS and RaLPS systems in figure 6. The case of RaLPS initially appears intriguing, as we see a substantial number of ice nuclei even within the extended sugar-water interface, where the water density is much lower than in the bulk of the water layer. This is indicative of high potency at nucleating ice of the RaLPS system but not inconsistent with the fact that ice cannot appear in under-coordinated water. In fact, water is not evenly dispersed within the sugar layer and, while the average water density is around $0.6\,g\,cm^{-3}$, this is arranged in pockets of fully coordinated water, see the ESI† for a visualisation of the RaLPS sugar distribution.

In summary, we have seen that DPPC-CHL/DMPI bilayers promote ice nucleation at the water-bilayer interface, albeit to a

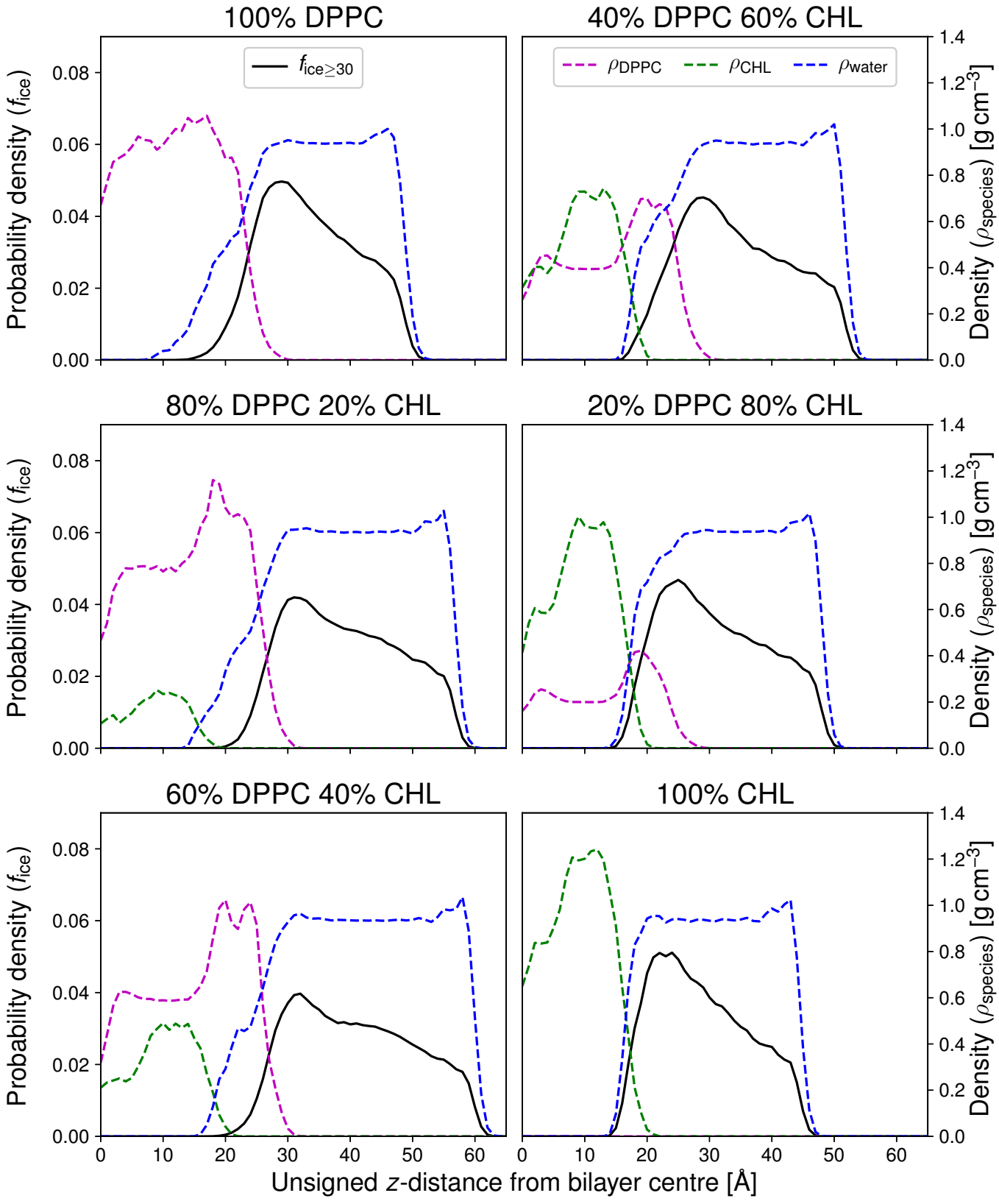

Fig. 4 Probability density $f_{ice}(z)$ (black, solid) for (unsigned) z-distance of water molecules, within a largest icy cluster, from the centre of mass of the bilayer. DPPC, CHL and water densities: $\rho_{DPPC}(z)$, $\rho_{CHL}(z)$ and $\rho_{water}(z)$ are displayed with dashed magenta, green and blue lines, respectively.

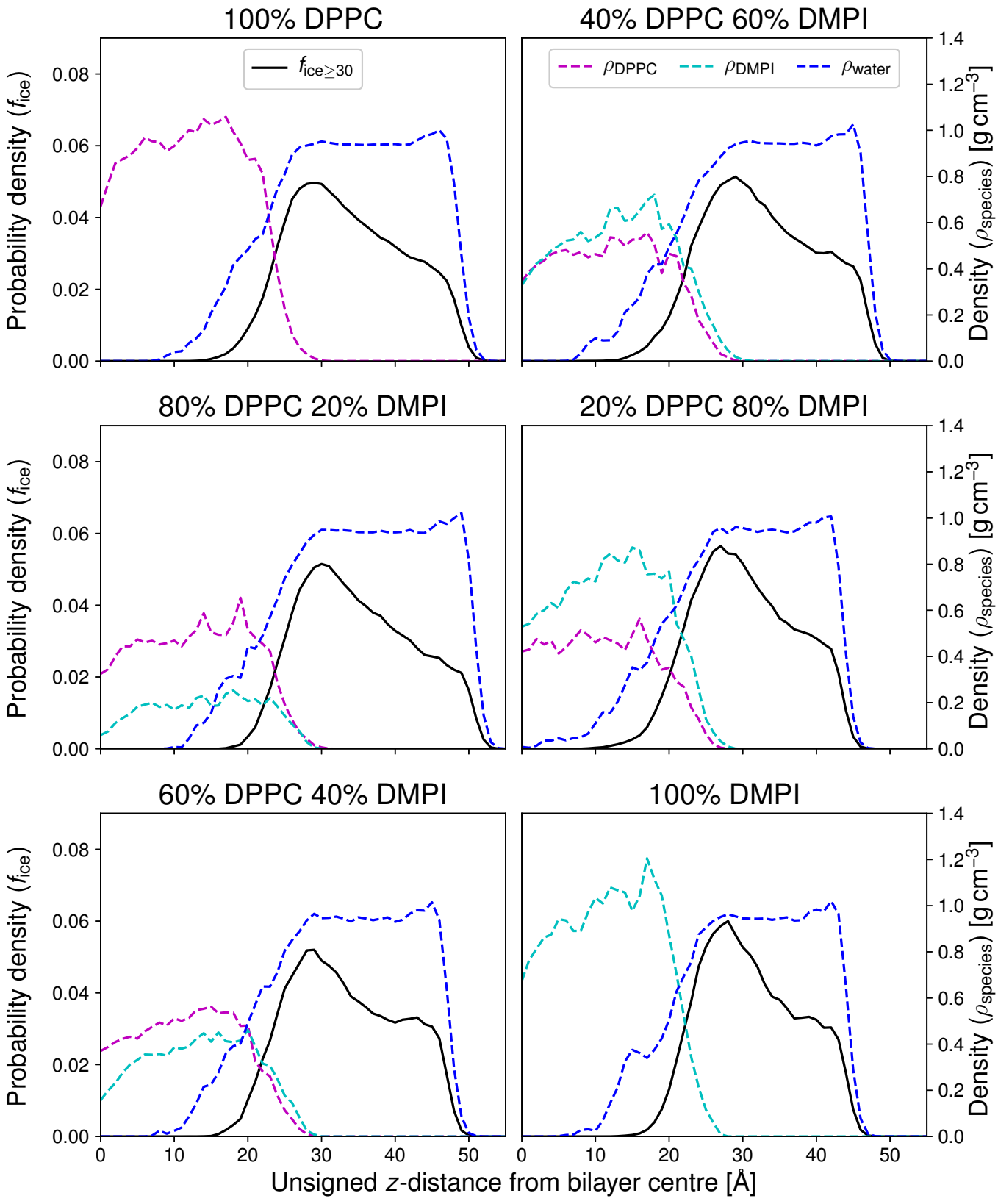

Fig. 5 Probability density $f_{ice}(z)$ (black, solid) for (unsigned) z-distance of water molecules, within a largest icy cluster, from the centre of mass of the bilayer. DPPC, DMPI and water densities: $\rho_{DPPC}(z)$, $\rho_{DMPI}(z)$ and $\rho_{water}(z)$ are displayed with dashed magenta, cyan and blue lines, respectively.

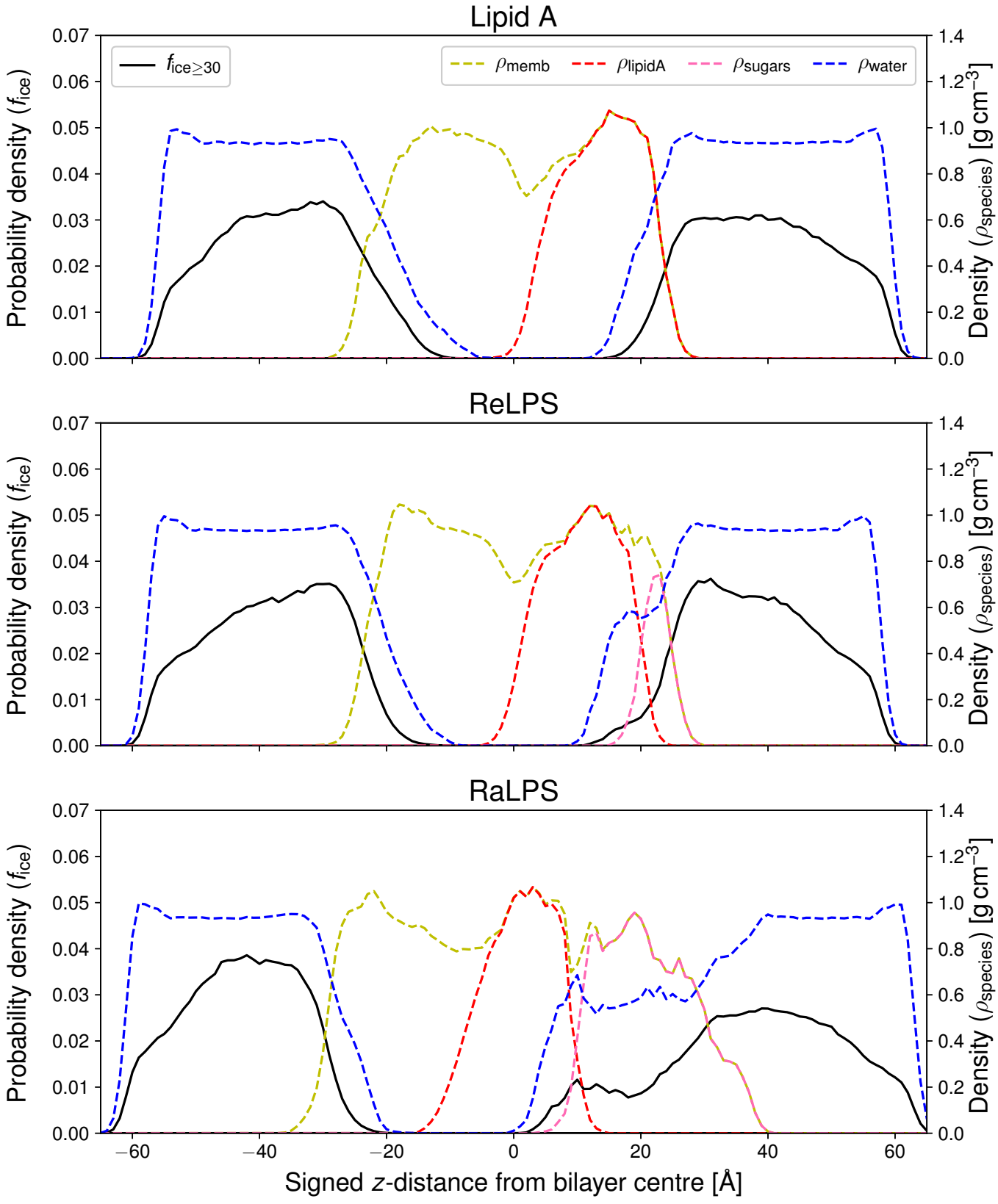

Fig. 6 Probability density $f_{ice}(z)$ (black, solid) for (signed) z-distance of water molecules, within a largest icy cluster, from the centre of mass of the bilayer. Total membrane, lipid A, sugar and water densities: $\rho_{memb}(z)$, $\rho_{lipidA}(z)$, $\rho_{sugars}(z)$ and $\rho_{water}(z)$ are displayed with dashed red, yellow, pink and blue lines, respectively.

much lesser extent than biological ice nucleating agents such as pollen or cholesterol crystals. In particular, homogeneous bilayers of DPPC, CHL and DMPI appear to have the largest such effect, although this is much more apparent in comparison with mixed DPPC-CHL bilayers than with DPPC-DMPI. We also saw that the sugar coatings of LPS membranes show some potential as ice nucleating agents. In the next section, we aim to explain some of these trends by investigating the structural properties of the bilayers.

3.2 Bilayer ordering

In order to characterise the structure, and particularly the degree of order within the different bilayers, we have utilised the SMAC parameter (see section 2.4.1). This quantity combines an indication of the local density of the lipids with a measure of the order within the bilayer. High (or low) values of the SMAC order parameter correspond to a higher (or lower) degree of order within the system. The results are summarised in Figure 7 as a function of the composition of the bilayer. For DPPC-CHL and DPPC-DMPI, we report the average values of the SMAC parameter for each lipid type as well as for the bilayers as a whole, whilst in the case of the (asymmetric) LPS systems, we report the value of the SMAC for the two leaflets of the bilayers separately.

In the case of the DPPC-CHL system, we observe that the addition of up to 40 mol% of CHL progressively increases the order within the bilayer, both for the DPPC and the CHL components. This effect is well-known[19,61,77] and seems to cease for CHL fractions higher than 40 mol%. In fact, pure DPPC and pure CHL bilayers are characterised by very similar degree of structural order — which is lower than any of the mixed systems. It is interesting to note that bilayers found in nature typically have CHL content ranging from 0–50 mol%[20,26]. These results are in (apparent) contradiction with the trends we have illustrated in figure 4, as the most ordered DPPC-CHL bilayers and particularly the 40 mol% CHL system show the weakest indication of the preference for the ice nuclei to form at the bilayer-water interface. In other words, the most ordered bilayers seem to display the weakest ice nucleating potential, which is in direct contradiction with our previous findings on CHL self-assembled monolayers[2], where we found that the ice nucleating ability of those systems is clearly directly proportional to the degree of structural order within the system. This conundrum will be addressed (and in fact, resolved) in the next section.

In contrast to the DPPC-CHL systems, DPPC-DMPI bilayers are characterised by very different structural trends as a function of the content of DMPI. Pure DPPC and pure DMPI are more ordered than any of the mixed systems, i.e. the opposite situation if compared with DPPC-CHL. Adding DMPI to DPPC induces a degree of structural disorder, which is largely due to the DMPI component, whilst the DPPC component displays very similar values of the SMAC parameter throughout the entire composition range. Again, this is a very different situation from what we have observed for DPPC-CHL, where the degree of order with respect to the DPPC and CHL components is very similar. The crucial difference between adding CHL and DMPI to DPPC is that CHL is much smaller than DPPC, whilst DMPI is very similar to DPPC (the only structural differences being located within the lipid headgroups). Given that the trend of DPPC-DMPI in terms of ice nucleating ability is similar to that of DPPC-CHL (see figure 5), this structural analysis appears even more confusing, as it is unclear why two systems with very different degrees of structural order should facilitate the formation of ice nuclei at the bilayer-water interface to a very similar extent. The key to this apparent contradiction is in the ability of these systems to form hydrogen bonds with the water phase, as we shall discuss in greater detail in the next section.

Another morphological property characterising the DPPC-CHL and DPPC-DMPI bilayers is the packing density. We can look at this simply by considering the box size, but in order to obtain a more insightful analysis we approximate the area per lipid via a Voronoi tessellation (see section 2.4.2). Figure 8 shows this Voronoi area per lipid for the DPPC-CHL and DPPC-DMPI systems. These values are higher for the DPPC-DMPI systems than

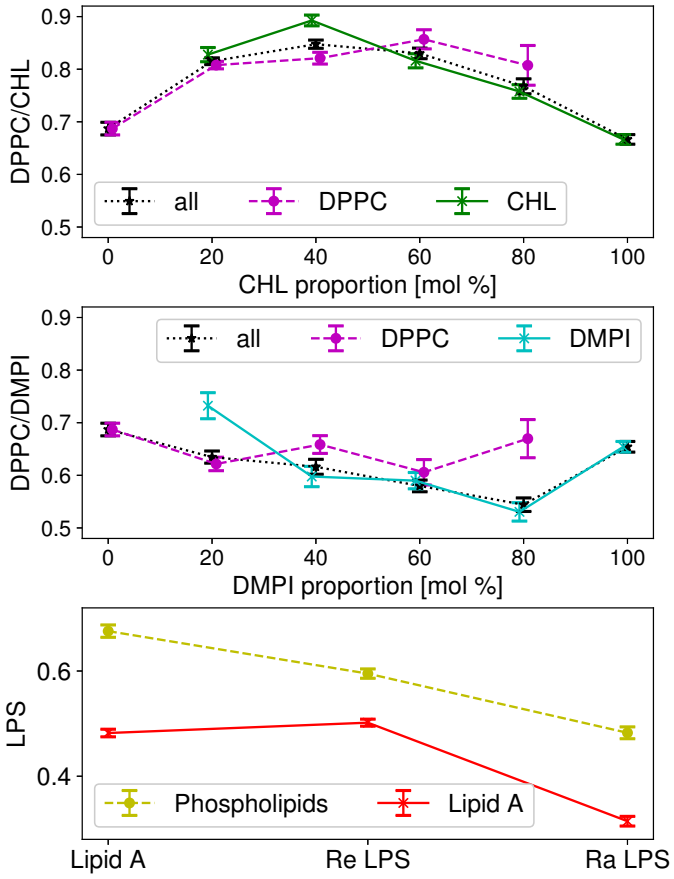

Fig. 7 Average SMAC parameter for lipid tails in different systems. The top panel shows SMAC for DPPC-CHL bilayers, with mol% CHL along the horizontal axis, the middle panel shows SMAC for DPPC-DMPI bilayers, with mol% DMPI along the horizontal axis, while the bottom panel shows SMAC for the three LPS bilayer systems. The error bars show one standard deviation. The points are slightly offset along the x-axis for improved readability. The y-scale is identical for DPPC-CHL and DPPC-DMPI for purposes of comparison, the scale is different for LPS due to the greatly lower degree of order in the lipid A tails.

for the DPPC-CHL systems; due to the fact that DMPI has a larger headgroup than DPPC, while CHL is significantly smaller. In the case of DPPC-CHL, the trends appear to correspond closely with the trends in SMAC, with DPPC taking up less space on average in the 40 mol% CHL system. An interesting observation is that CHL has a similar Voronoi area per lipid across all systems except for the 20 mol% CHL system, where the area per lipid computed is significantly lower. In the DPPC-DMPI systems, the trend is broadly linear, increasing with mol% DMPI, this can be simply explained by the fact that DMPI has a larger headgroup than DPPC.

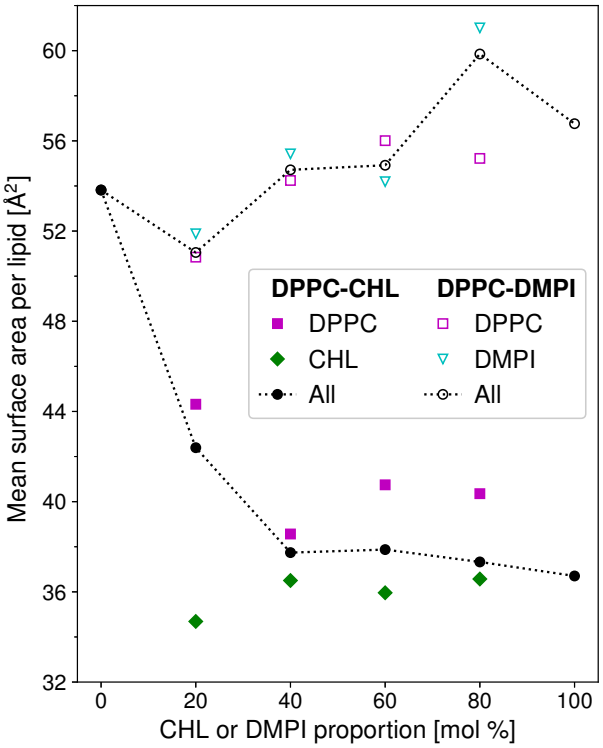

Fig. 8 Average (Voronoi) surface area per lipid. DPPC-CHL systems have solid points, DPPC-DMPI have unfilled points.

We have not computed Voronoi areas for the LPS systems since the differences between those systems are along the z-axis and not in the xy-plane. However the average surface area per lipid A molecule can be calculated by simply taking the cross-sectional area of the box and dividing by the number of molecules, this gives average lipid A areas per lipid of 157.6, 169.7 and 180.2 Å^2 for the Lipid A, ReLPS and RaLPS systems respectively. In the LPS systems, the addition of sugars to lipid A (i.e. from Lipid A, with no sugars, to ReLPS and RaLPS with the most extended sugar coating) results in an only marginal increase in terms of its order within ReLPS compared to pure (i.e. no sugars) Lipid A and a much more noticeable disordering effect for lipid A within RaLPS. Note that in every LPS system, lipid A is far more disordered than any component within DPPC-CHL or DPPC-DMPI systems. The fact that the phospholipids leaflets appear to be less ordered as we move from Lipid A to ReLPS and RaLPS is partially due to the increasing surface area per lipid, causing the SMAC to be lower. Overall, the LPS systems are much more disordered than the DPPC-CHL and DPPC-DMPI bilayers. We have seen that Lipid A alone is not effective at all in facilitating the emergence of ice nuclei at the interface with the bilayer. However, the even more disordered ReLPS, and particularly RaLPS, display some potential as ice nucleating agents. This is despite the fact that defining a set of molecular axis to compute a meaningful value of the SMAC order parameter for the very disordered sugars fraction involved with ReLPS and RaLPS is not even possible.

Having explored the structural differences between the systems under consideration, we will move in the next section onto a discussion of the interactions between the bilayers and the water phase, studying the hydrogen bonds between the two.

3.3 Hydrogen bonding

The ability of a given surface to form hydrogen bonds with water is an important factor in determining its ice nucleating activity[1,64,78,79]. As an example, we have previously identified the amphiphilicity (i.e. the ability to act as both hydrogen bond acceptor or donor) of the −OH groups of CHL to be crucial to its ice nucleating potential[1,2], albeit the structure of the surface itself can play an even more important role (with ordered crystals being much more efficient that self-assembled monolayers). In this section, we investigate the emergence of hydrogen bonds between our bilayers and the water phase.

The results are summarised in Figure 9, which illustrates the average number of hydrogen bonds between each bilayer and the largest icy cluster per frame (see section 2.3) as a function of the bilayer composition. For the DPPC-CHL and DPPC-DMPI systems, hydrogen bonds are reported by bonding site (see figure 1) and whether the hydrogen bond is donated or accepted by the bilayer, if applicable. For the LPS systems, the hydrogen bonds are reported with reference to each residue instead.

We begin with the DPPC-CHL systems. In this case, the number of hydrogen bonds between the largest icy clusters and the CHL molecules is proportional to the CHL content. Only a negligible number of hydrogen bonds form below 40 mol% CHL, though, as for such small fractions the CHL molecules tend to sit very close to the centre of the bilayer, thus becoming inaccessible to the water phase. This trend can be appreciated by observing that, as illustrated in figure 4, for the 20 and 40 mol% CHL systems there is very little overlap between the extent of the population of the icy clusters along the z-direction and the CHL density. In turn, this is due to the low water density so far into the bilayer-water interface, where the DPPC density is conversely quite high.

Trends for hydrogen bonds between water and DPPC are less clear, fluctuating rather than showing any clear connection to the content of DPPC. DPPC has eight hydrogen bonding sites (see figure 1), of which five are especially deep within the bilayer-water interface (the four “tailgroup oxygens” and the innermost phosphate oxygen). As such, the increased water density around these sites increases the total number of hydrogen bonds even

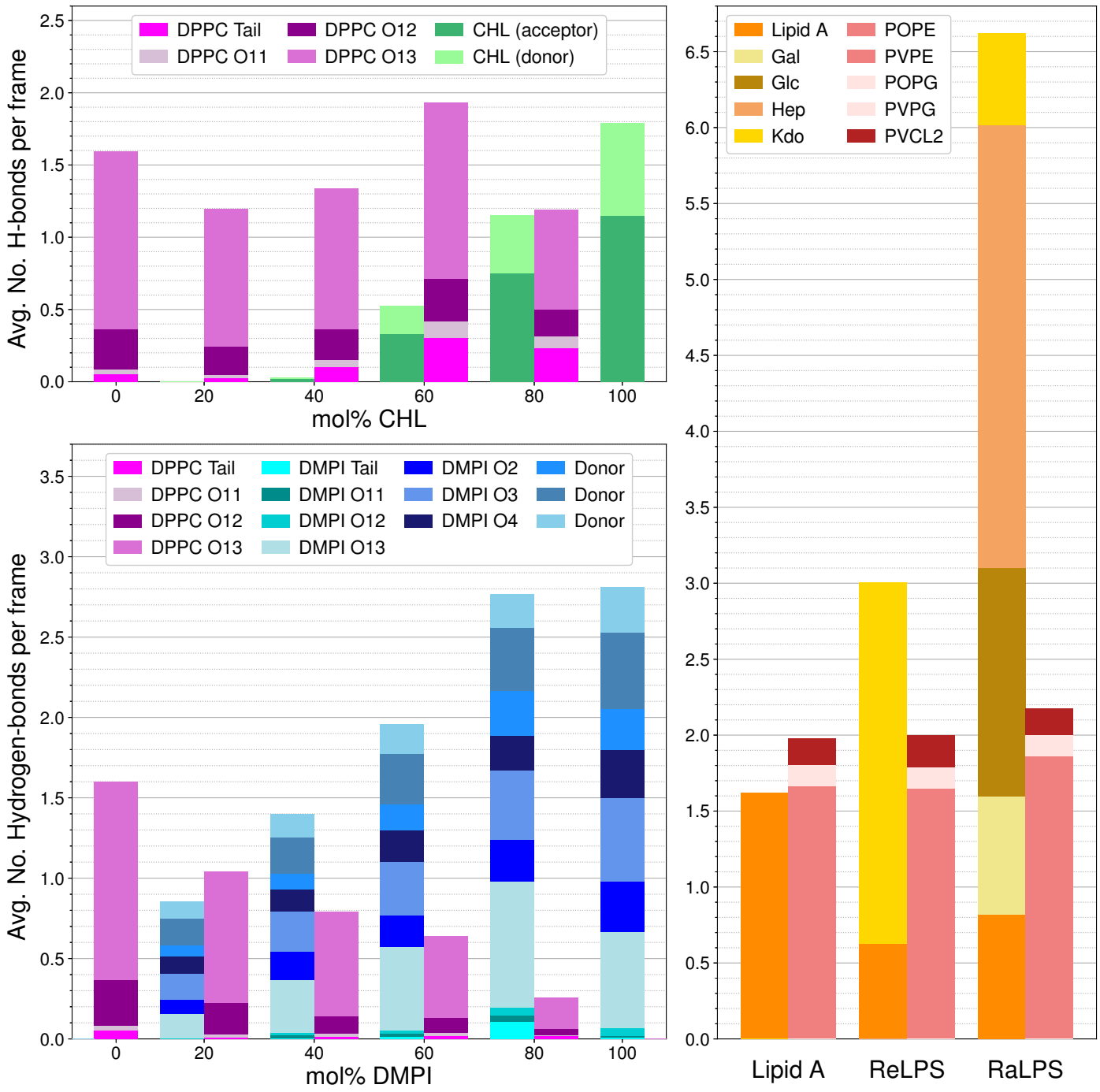

Fig. 9 Average number of hydrogen bonds per frame from the largest icy cluster to DPPC-CHL (top left), DPPC-DMPI (bottom left) and LPS (right) bilayers. For DPPC, CHL and DMPI, the different possible bonding sites are coloured in the same way as in figure 1. For the LPS systems, bonding sites are grouped by molecule and not distinguished between donors and acceptors.

as the DPPC proportion decreases; we see this trend clearly in figure 9, with the two lowest bars peaking at 60 mol% CHL. While this effect of water density around bonding sites versus actual number of bonding sites is clearest for these five sites, it seems logical that a similar but smaller effect is present for the other three bonding sites, which are all partially submerged within the bilayer.

Crucially, these results explain the apparent contradiction we have highlighted in the previous section. DPPC-CHL bilayers with 20 and 40 mol% CHL are the most ordered (due to the structural, "condensing" effect[61,77] of CHL), but because the CHL hydrogen bonding sites are inaccessible to the water phase, the ice nucleating potential of these systems as a whole is inferior to that of e.g. the pure DPPC or CHL bilayers, despite the fact that the latter are less ordered than any of the mixed systems.

The situation is somewhat different for the DPPC-DMPI systems. As these two lipids are much more similar to each other in comparison to the differences between DPPC and CHL, the number of hydrogen bonds between either DPPC or DMPI and the icy clusters is proportional to the composition of each lipid. The one exception to this trend can be observed at either end of the mol% DMPI range: both the 20 and 80 mol% DMPI systems clearly show a higher number of hydrogen bonds than one would expect from a linear relationship between lipid content and number of hydrogen bonds. This can be explained by considering the differences between the DPPC and DMPI headgroups: the DMPI headgroup is larger than the DPPC one and characterised by a considerably higher number of hydrogen bonding sites. As such, the higher-than-expected number of hydrogen bonds for 20 and 80 mol% DMPI systems is most likely due to increased water density around the DMPI headgroup hydrogen bonding sites.

It is also evident that DMPI forms, on average, more hydrogen bonds with the icy clusters than DPPC. This can be attributed to the far greater number of bonding sites: thirteen, in the case of DMPI, five of which can donate or accept hydrogen bonds, compared to eight for DPPC — which can only act as a hydrogen bond acceptor. Interestingly, these results in terms of the hydrogen bonding are entirely consistent with the slightly higher ice nucleating activity of pure DMPI as compared to pure DPPC (see figures 4 and 5). Note that, in contrast to DPPC-CHL bilayers, mixed DPPC-DMPI are more disordered than the pure components (see figures 7 and 8); however, the higher potential of DMPI to facilitate hydrogen bonds between the bilayer and the water phase, explains why even fairly disordered mixed DPPC-DMPI systems display ice nucleating potential which is equal or greater than their DPPC-CHL counterparts.

In the case of the LPS systems, the number of hydrogen bonds between the phospholipid leaflet and water is, as expected, very similar across the different bilayers. Stark differences can instead be observed between the LPS leaflets, where the hydrogen bonding increases as a function of the amount of sugars in the system. This is consistent with the evidence we have reported in figure 6. In contrast with the ReLPS and RaLPS systems, the Lipid A system does not facilitate the formation of ice nuclei at the water-bilayer interface. The latter in particular forms a large number of hydrogen bonds between the Hep residues within the sugar coating and the water, within a region where the water density is in fact quite low. In the RaLPS system, and to a lesser extend the ReLPS system, we note that we have a greatly increased surface area and therefore number of accessible hydrogen bonds, due to the way that the sugars sit within the water. It is particularly interesting to observe that lipid A forms more hydrogen bonds in the RaLPS system than in the ReLPS system, despite reduced accessibility to its bonding sites; this suggests that RaLPS acts as an especially potent ice nucleating surface.

In summary, this analysis highlights the importance of the interplay between the hydrogen bonding potential of the individual components of the bilayer and the structural order of the membrane. Specifically, there is a clear correlation between the extent of hydrogen bonding and the ability of the bilayer to induce the formation of ice nuclei at its interface with water. However, it is key for the water phase to be able to access the hydrogen bonding sites of the different components within a given bilayer. In the next section we will build on these results, exploring the connection between hydrogen bonding and the orientation of the water molecules at the interface with the bilayers.

3.4 Water orientation

It is widely accepted that the structure of liquid water can be severely affected by the presence of both hydrophobic and hydrophilic surfaces[80]. This "structuring" effect has also been put forward as a key factor regarding the ice nucleating ability of a given surface[81,82]. Here, we focus on the orientational order of the water molecules, as a function of their distance from the centre of the bilayers. In particular, we have investigated the changes in the average value of the angle θ defined by the water dipole moment and the z-axis of the simulation box (perpendicular to the bilayers plane). The results are reported in Figures 10 and 11 as color maps, in conjunction with the density of the water phase — also as a function of the distance from the centre of the bilayer. As expected, the average value of θ in the "bulk region" of the water phase, that is, far enough from the bilayer, is 90°. This result provides further evidence that our simulated water layer is thick enough to behave as bulk water, as discussed in greater detail in the ESI.[†]

A rather interesting trend can be observed for the DPPC-CHL systems: for pure DPPC, θ is on average lower than 90°, which indicates that the dipole moment of the water molecules tends to point toward the bilayer (see figure 3). This is consistent with the fact that all of the hydrogen bonding sites on DPPC are acceptors. As the CHL content increases, however, the average value of θ at the water-bilayer interface progressively moves toward values higher than 90°. This behaviour can be explained by noticing that the $-$OH groups of CHL can act as both acceptors and donors for hydrogen bonds. For DPPC-DMPI systems, the average values of θ remains below 90° across the entire composition range. This is because many DMPI hydrogen bonding sites are, like DPPC, acceptors only.

In the case of the LPS systems, the extent of the hydration layers, particularly for the sugar-coated ReLPS and RaLPS, results in a low-density water region that makes any quantitative assess-

ment of the average orientation of the water molecules rather challenging. Overall, we do observe a tendency for lipid A alone, as well as the phospholipid leaflet alone, to display similar trends as pure DPPC or DMPI. What is interesting is the fact that ReLPS and particularly RaLPS appear to still be able to facilitate ice nucleation (see Figure 6) despite the absence of water structuring and the extent of the hydration layer.

4 Conclusions

Exploring the possibility that lipid bilayers, the building blocks of cellular membranes, can act as ice nucleating agents is key to furthering our understanding of the microscopic mechanisms ruling the current and future cryopreservation protocols. This is especially true when adopting slow-freezing techniques, given the fact that ice nucleation appears to occur at very mild supercooling — or at far warmer temperatures than those associated with the onset of homogeneous ice nucleation.

In this work, we have investigated the ice nucleating ability of three classes of lipid bilayers across a range of different compositions, by quantifying the tendency for pre-critical ice nuclei to form at the water-bilayer interface. We have found that most of these lipid bilayers display some potential as ice nucleating agents. By comparing our results with those we have obtained (and cross-validated with experimental evidence) for CHL crystals [1] as well as self-assembled monolayers [2], we argue that the ice nucleating activity of these bilayers is bound to be much weaker than that of the most effective biological agents; such as some varieties of pollen, some steroid crystals or specific bacterial fragments. [71–76]

Interestingly, the ice nucleating ability of single-component bilayers, e.g. DPPC, CHL and DMPI only, appears to be slightly stronger than what we have observed for mixed systems. This is due to the interplay between the structural order of the bilayer and the ability of the individual components to form hydrogen bonds with water. For instance, DMPI is more active than both DPPC and CHL — due to its higher number of hydrogen bonding sites per molecule. However, we have identified the accessibility of these hydrogen bonding sites to be paramount in facilitating the emergence of ice nuclei at the bilayer-water interface. In mixed systems, some components might be buried deep in the bilayer, thus preventing the water from reaching those hydrogen bonding sites in the first place. For instance, the addition of CHL in DPPC bilayer substantially increases the structural order of the whole system: however, the CHL molecules sit in the middle of the bilayer, away from the hydration layer and thus lowering the overall density of available hydrogen bonding sites within the system.

In addition, we have found that sugar-coated lipids show some potential as ice nucleating agents as well. This is important, as bacterial and animal cellular membranes are more often than not coated with a sugar phase (which forms the so-called pericellular matrix). While lipid A alone appears to have no impact at all on the formation of ice nuclei (despite offering multiple, accessible hydrogen bonding sites), both the ReLPS and even more so the RaLPS system display a strong tendency to facilitate the emergence of ice nuclei within the hydration layer. This is surprising, as the sugar phase is very disordered and generates an extended hydration layer where the water density is quite low. On the other hand, some residues within the sugar phase offer a substantial number of hydrogen bonding sites. These considerations are also reflected in the structuring of the water phase at the interface with the bilayers, which we have quantified by looking at the orientation of the water molecules as a function of their distance from the centre of the bilayer.

As a whole, our findings suggest that, while the building blocks of cellular membranes do display some potential as ice nucleating agents (including the sugar-coated systems), it is likely that other entities are responsible for the onset of ice nucleation at the mild supercooling reported in the context of cryopreservation protocols. Whilst the quest to identify what exactly is responsible to trigger ice nucleation when dealing with slow-freezing approaches remains unanswered, we have elucidated the interplay between structural order, hydrogen bonding potential and, crucially, the accessibility of the hydrogen bonding sites as the key factors at the heart of the ice nucleating ability of lipid bilayers. These findings represent a step forward toward a more complete understanding of heterogeneous ice nucleation in biological matter and call for further work aimed at the systematic investigation of a diverse portfolio of biological compounds at the molecular level.

Author Contributions

G.S. and A.D. conceived the research. C.M. performed the MD simulations and analysed the results. All authors have contributed to the analysis of the results and their discussion. P.-C.H. and S.K. provided structural information about LPS systems. C.M. and G.S. wrote the manuscript.

Conflicts of interest

There are no conflicts to declare.

Acknowledgements

C.M. thanks EPSRC for a Ph.D. studentship through the EPSRC Centre for Doctoral Training in Molecular Analytical Science, grant number EP/L015307/1. The authors acknowledge high performance computing facilities provided by the Scientific Computing Research Technology Platform of the University of Warwick; the use of Athena HPC Midlands+, funded by the EPSRC, grant number EP/P020232/1; and the use of the national supercomputing service, ARCHER, granted via the UK High-End Computing Consortium for Biomolecular Simulation, HECBioSim, supported by EPSRC, grant number EP/R029407/1. We also acknowledge the use of hydrogen bond analysis code written by Matthew Warren.

References

1 G. C. Sosso, T. F. Whale, M. A. Holden, P. Pedevilla, B. J. Murray and A. Michaelides, *Chem. Sci.*, 2018, **9**, 8077–8088.

2 G. C. Sosso, P. Sudera, A. T. Kunert, T. F. Whale, J. Fröhlich-Nowoisky, M. Bonn, A. Michaelides and E. H. G. Backus, *Chem. Sci.*, submitted.

3 C. Miyagi-Shiohira, K. Kurima, N. Kobayashi, I. Saitoh,

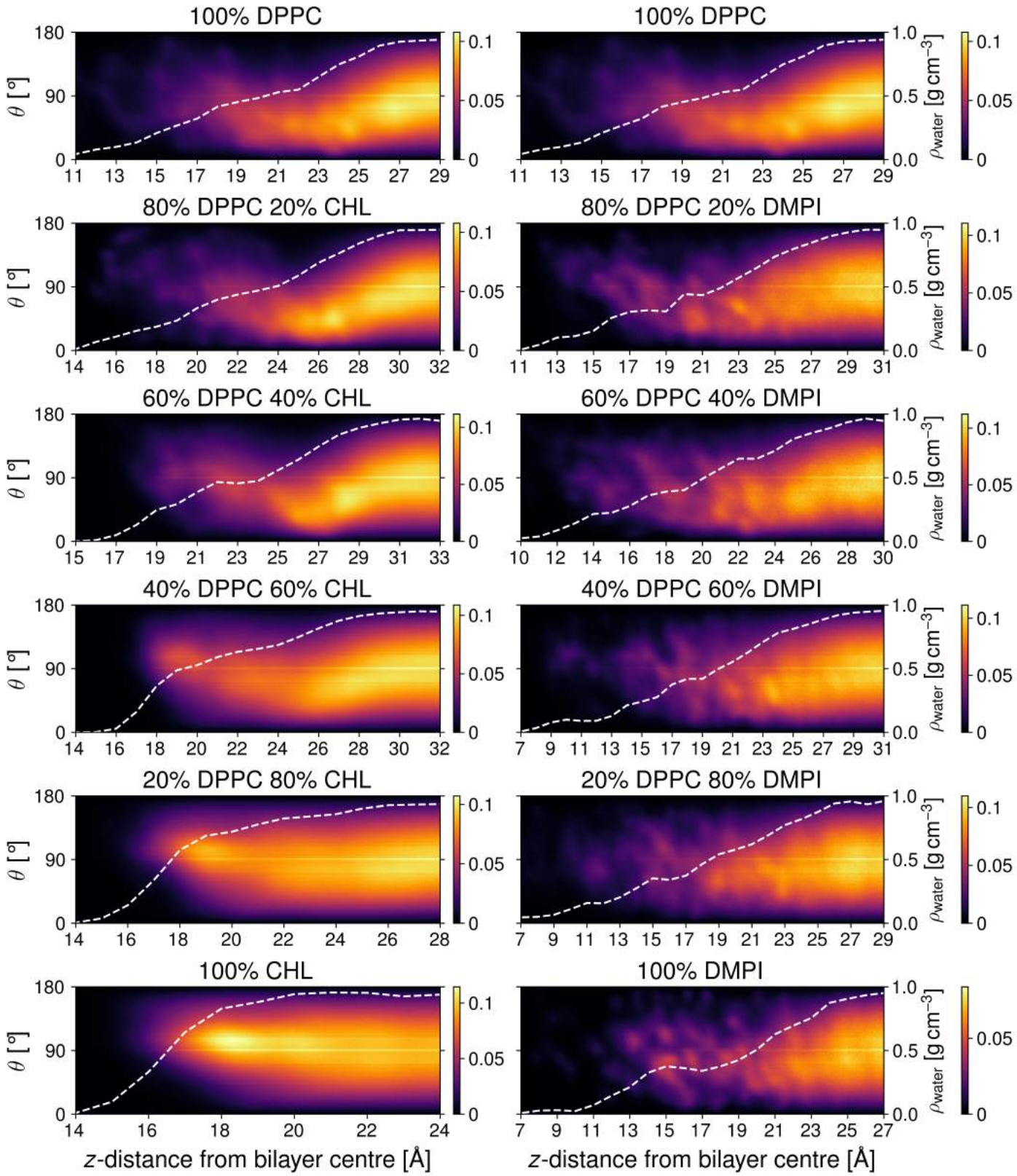

Fig. 10 Orientational order parameter (θ) colour maps for DPPC-CHL/DMPI systems (see section 2.5). Average water density is shown as a dashed white line. The scale for the colour map is count per frame per $Å^3$ per $180°$. A value of $\theta = 0°$ corresponds to the dipole moment pointing away from the plane of the bilayer (along the normal) while a value of $\theta = 180°$ corresponds to the dipole moment pointing towards the plane of the bilayer.

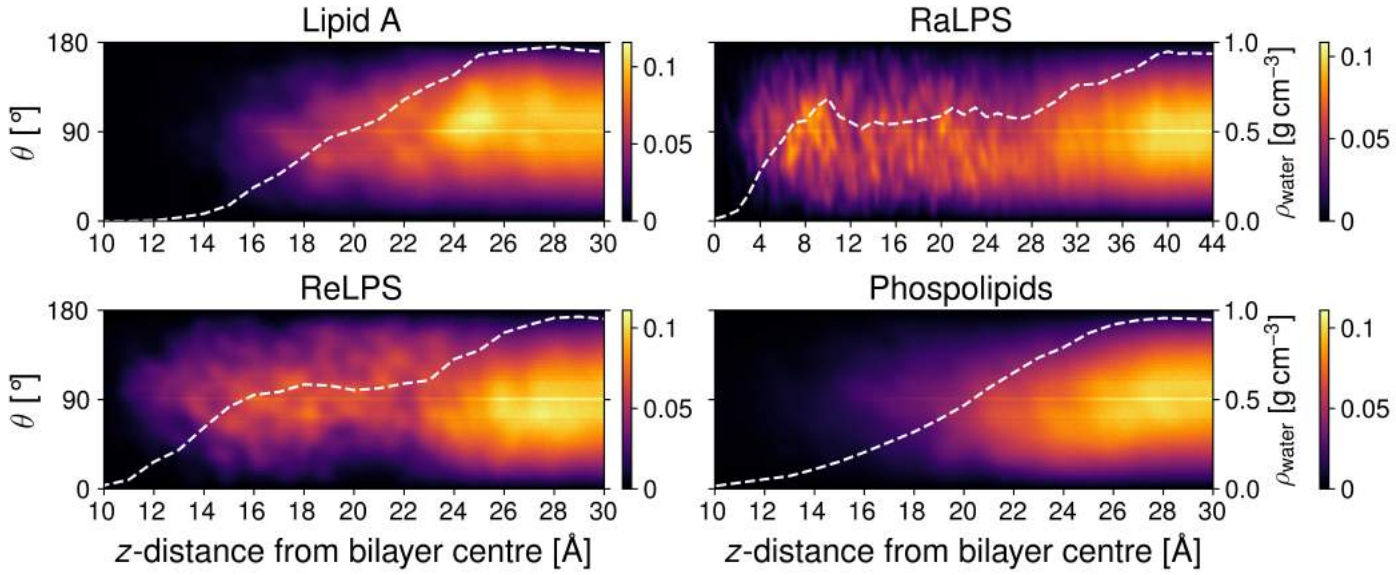

Fig. 11 Orientational order parameter (θ) colour maps for LPS systems (see section 2.5). Average water density is shown as a dashed white line. The scale for the colour map is count per frame per Å^3 per 180°. A value of $\theta = 0°$ corresponds to the dipole moment pointing away from the plane of the bilayer (along the normal) while a value of $\theta = 180°$ corresponds to the dipole moment pointing towards the plane of the bilayer.

M. Watanabe, Y. Noguchi, M. Matsushita and H. Noguchi, *Cell Med.*, 2015, **8**, 3.

4 K. W. Yong, B. Pingguan-Murphy, F. Xu, W. A. B. Wan Abas, J. R. Choi, S. Z. Omar, M. A. N. Azmi, K. H. Chua and W. K. Z. Wan Safwani, *Sci. Rep.*, 2015, **5**, 9596.

5 O. Maslova, M. Novak and P. Kruzliak, *Stem Cells Int.*, 2015, **2015**, 150609.

6 D. E. Pegg, *Methods Mol. Biol.*, 2007, **368**, 39–57.

7 L. E. McGann, H. Yang and M. Walterson, *Cryobiology*, 1988, **25**, 178–185.

8 D. Gao and A. K. Critser, *ILAR J.*, 2000, **41**, 187–196.

9 T. H. Jang, S. C. Park, J. H. Yang, J. Y. Kim, J. H. Seok, S. Park, C. W. Choi, S. R. Lee and J. Han, *Integr. Med. Res.*, 2017, **6**, 12–18.

10 K. W. Yong, W. K. Z. Wan Safwani, F. Xu, W. A. B. Wan Abas, J. R. Choi and B. Pingguan-Murphy, *Biopreserv. Biobank.*, 2015, **13**, 231–239.

11 A. A. Mandawala, S. C. Harvey, T. K. Roy and K. E. Fowler, *Theriogenology*, 2016, **86**, 1637–1644.

12 T. Duong, R. Barrangou, W. M. Russell and T. R. Klaenhammer, *Appl. Environ. Microbiol.*, 2006, **72**, 1218.

13 N. K. Jain and I. Roy, *Protein Sci.*, 2009, **18**, 24–36.

14 D. E. Mitchell, A. E. R Fayter, R. C. Deller, M. Hasan, J. Gutierrez-Marcos and M. I. Gibson, *Mater. Horizons*, 2019, **6**, 364.

15 E. Mocé, E. Blanch, C. Tomás and J. Graham, *Reprod. Domest. Anim.*, 2010, **45**, 57–66.

16 I. Massie, C. Selden, H. Hodgson and B. Fuller, *Tissue Eng. Part C. Methods*, 2011, **17**, 765–774.

17 S. J. McKinnon, S. L. Whittenburg and B. Brooks, *J. Phys. Chem.*, 1992, **96**, 10497–10506.

18 C. Hofsäß, E. Lindahl and O. Edholm, *Biophys. J.*, 2003, **84**, 2192–2206.

19 T. Róg, M. Pasenkiewicz-Gierula, I. Vattulainen and M. Karttunen, *Biochim. Biophys. Acta - Biomembr.*, 2009, **1788**, 97–121.

20 G. M. Cooper, *The Cell: A Molecular Approach*, Sinauer Associates, Sunderland (MA), 2nd edn, 2000.

21 T. J. Silhavy, D. Kahne and S. Walker, *Cold Spring Harb. Perspect. Biol.*, 2010, **2**, a000414.

22 P. C. Hsu, F. Samsudin, J. Shearer and S. Khalid, *J. Phys. Chem. Lett.*, 2017, **8**, 5513–5518.

23 H. M.-S. Monne, R. Danne, T. Róg, V. Ilpo and A. Gurtovenko, *Biophys. J.*, 2013, **104**, 251a.

24 F. Cochet and F. Peri, *Int. J. Mol. Sci.*, 2017, **18**, 2318.

25 P. C. Hsu, B. M. Bruininks, D. Jefferies, P. Cesar Telles de Souza, J. Lee, D. S. Patel, S. J. Marrink, Y. Qi, S. Khalid and W. Im, *J. Comput. Chem.*, 2017, **38**, 2354–2363.

26 B. Alberts, A. Johnson, J. Lewis, M. Raff, K. Roberts and P. Walter, *Molecular Biology of the Cell*, Garland Science, New York, 4th edn, 2002.

27 R. B. Head, *Nature*, 1961, **191**, 1058–1059.

28 S. Jo, T. Kim, V. G. Iyer and W. Im, *J. Comput. Chem.*, 2008, **29**, 1859–1865.

29 B. R. Brooks, C. L. Brooks, A. D. Mackerell, L. Nilsson, R. J. Petrella, B. Roux, Y. Won, G. Archontis, C. Bartels, S. Boresch, A. Caflisch, L. Caves, Q. Cui, A. R. Dinner, M. Feig, S. Fischer, J. Gao, M. Hodoscek, W. Im, K. Kuczera, T. Lazaridis, J. Ma, V. Ovchinnikov, E. Paci, R. W. Pastor, C. B. Post, J. Z. Pu, M. Schaefer, B. Tidor, R. M. Venable, H. L. Woodcock, X. Wu, W. Yang, D. M. York and M. Karplus, *J. Comput. Chem.*, 2009, **30**, 1545–1614.

30 J. Lee, X. Cheng, J. M. Swails, M. S. Yeom, P. K. Eastman, J. A. Lemkul, S. Wei, J. Buckner, J. C. Jeong, Y. Qi, S. Jo, V. S.

Pande, D. A. Case, C. L. Brooks, A. D. MacKerell, J. B. Klauda and W. Im, *J. Chem. Theory Comput.*, 2016, **12**, 405–413.
31 E. L. Wu, X. Cheng, S. Jo, H. Rui, K. C. Song, E. M. Dávila-Contreras, Y. Qi, J. Lee, V. Monje-Galvan, R. M. Venable, J. B. Klauda and W. Im, *J. Comput. Chem.*, 2014, **35**, 1997–2004.
32 S. Jo, J. B. Lim, J. B. Klauda and W. Im, *Biophys. J.*, 2009, **97**, 50–58.
33 H. J. Berendsen, D. van der Spoel and R. van Drunen, *Comput. Phys. Commun.*, 1995, **91**, 43–56.
34 E. Lindahl, B. Hess and D. van der Spoel, *J. Mol. Model.*, 2001, **7**, 306–317.
35 D. Van Der Spoel, E. Lindahl, B. Hess, G. Groenhof, A. E. Mark and H. J. Berendsen, *J. Comput. Chem.*, 2005, **26**, 1701–1718.
36 B. Hess, C. Kutzner, D. Van Der Spoel and E. Lindahl, *J. Chem. Theory Comput.*, 2008, **4**, 435–447.
37 S. Pronk, S. Páll, R. Schulz, P. Larsson, P. Bjelkmar, R. Apostolov, M. R. Shirts, J. C. Smith, P. M. Kasson, D. Van Der Spoel, B. Hess and E. Lindahl, *Bioinformatics*, 2013, **29**, 845–854.
38 S. Páll, M. J. Abraham, C. Kutzner, B. Hess and E. Lindahl, Solving Softw. Challenges Exascale, 2015, pp. 3–27.
39 M. J. Abraham, T. Murtola, R. Schulz, S. Páll, J. C. Smith, B. Hess and E. Lindah, *SoftwareX*, 2015, **1-2**, 19–25.
40 K. Vanommeslaeghe, E. Hatcher, C. Acharya, S. Kundu, S. Zhong, J. Shim, E. Darian, O. Guvench, P. Lopes, I. Vorobyov and A. D. Mackerell, *J. Comput. Chem.*, 2010, **31**, 671–690.
41 K. Vanommeslaeghe and A. D. MacKerell, *J. Chem. Inf. Model.*, 2012, **52**, 3144–3154.
42 K. Vanommeslaeghe, E. P. Raman and A. D. MacKerell, *J. Chem. Inf. Model.*, 2012, **52**, 3155–3168.
43 W. Yu, X. He, K. Vanommeslaeghe and A. D. MacKerell, *J. Comput. Chem.*, 2012, **33**, 2451–2468.
44 I. Soteras Gutiérrez, F. Y. Lin, K. Vanommeslaeghe, J. A. Lemkul, K. A. Armacost, C. L. Brooks and A. D. MacKerell, *Bioorganic Med. Chem.*, 2016, **24**, 4812–4825.
45 J. B. Klauda, R. M. Venable, J. A. Freites, J. W. O'Connor, D. J. Tobias, C. Mondragon-Ramirez, I. Vorobyov, A. D. MacKerell and R. W. Pastor, *J. Phys. Chem. B*, 2010, **114**, 7830–7843.
46 J. L. Abascal, E. Sanz, R. G. Fernández and C. Vega, *J. Chem. Phys.*, 2005, **122**, 234511.
47 D. R. Nutt and J. C. Smith, *J. Chem. Theory Comput.*, 2007, **3**, 1550–1560.
48 U. S. Midya and S. Bandyopadhyay, *J. Phys. Chem. B*, 2014, **118**, 4743–4752.
49 S. Miyamoto and P. A. Kollman, *J. Comput. Chem.*, 1992, **13**, 952–962.
50 B. Hess, H. Bekker, H. J. Berendsen and J. G. Fraaije, *J. Comput. Chem.*, 1997, **18**, 1463–1472.
51 S. Leekumjorn and A. K. Sum, *Biochim. Biophys. Acta - Biomembr.*, 2007, **1768**, 354–365.
52 D. Bostick and M. L. Berkowitz, *Biophys. J.*, 2003, **85**, 97–107.
53 J. R. Espinosa, C. Vega and E. Sanz, *J. Phys. Chem. C*, 2016, **120**, 8068–8075.
54 P. J. Steinhardt, D. R. Nelson and M. Ronchetti, *Phys. Rev. B*, 1983, **28**, 784–805.
55 The PLUMED Consortium, *Nat. Methods*, 2019, **16**, 670–673.
56 G. A. Tribello, M. Bonomi, D. Branduardi, C. Camilloni and G. Bussi, *Comput. Phys. Commun.*, 2014, **185**, 604–613.
57 M. Bonomi, D. Branduardi, G. Bussi, C. Camilloni, D. Provasi, P. Raiteri, D. Donadio, F. Marinelli, F. Pietrucci, R. A. Broglia and M. Parrinello, *Comput. Phys. Commun.*, 2009, **180**, 1961–1972.
58 F. Giberti, M. Salvalaglio, M. Mazzotti and M. Parrinello, *Chem. Eng. Sci.*, 2015, **121**, 51–59.
59 F. Giberti, M. Salvalaglio, M. Parrinello and E. Zurich, *IUCrJ*, 2015, **2 (Pt2)**, 256–266.
60 S. A. Pandit, S. Vasudevan, S. W. Chiu, R. J. Mashl, E. Jakobsson and H. L. Scott, *Biophys. J.*, 2004, **87**, 1092–1100.
61 F. Leeb and L. Maibaum, *Biophys. J.*, 2018, **115**, 2179–2188.
62 S. Buchoux, *Bioinformatics*, 2017, **33**, 133–134.
63 Y. Zhang, A. Lervik, J. Seddon and F. Bresme, *Chem. Phys. Lipids*, 2015, **185**, 88–98.
64 Y. Bi, R. Cabriolu and T. Li, *J. Phys. Chem. C*, 2016, **120**, 1507–1514.
65 M. Fitzner, G. C. Sosso, S. J. Cox and A. Michaelides, *J. Am. Chem. Soc.*, 2015, **137**, 13658–13669.
66 G. C. Sosso, J. Chen, S. J. Cox, M. Fitzner, P. Pedevilla, A. Zen and A. Michaelides, *Chem. Rev.*, 2016, **116**, 7078–7116.
67 Y. Qiu, N. Odendahl, A. Hudait, R. Mason, A. K. Bertram, F. Paesani, P. J. DeMott and V. Molinero, *J. Am. Chem. Soc.*, 2017, **139**, 3052–3064.
68 D. A. Knopf, P. A. Alpert and B. Wang, *ACS Earth Sp. Chem.*, 2018, **2**, 168–202.
69 G. C. Sosso, T. Li, D. Donadio, G. A. Tribello and A. Michaelides, *J. Phys. Chem. Lett.*, 2016, **7**, 2350–2355.
70 G. C. Sosso, G. A. Tribello, A. Zen, P. Pedevilla and A. Michaelides, *J. Chem. Phys.*, 2016, **145**, 211927.
71 L. R. Maki, E. L. Galyan, M.-M. Chang-Chien and D. R. Caldwell, *Appl. Microbiol.*, 1974, **28**, 456.
72 G. G. de Araujo, F. Rodrigues, F. L. T. Gonçalves and D. Galante, *Sci. Rep.*, 2019, **9**, 7768.
73 B. G. Pummer, H. Bauer, J. Bernardi, S. Bleicher and H. Grothe, *Atmos. Chem. Phys.*, 2012, **12**, 2541–2550.
74 K. Dreischmeier, C. Budke, L. Wiehemeier, T. Kottke and T. Koop, *Sci. Reports 2017 71*, 2017, **7**, 1–13.
75 E. Gute and J. P. Abbatt, *Atmos. Environ.*, 2020, **231**, 117488.
76 E. Gute, R. O. David, Z. A. Kanji and J. P. D. Abbatt, *ACS Earth Sp. Chem.*, 2020, **4**, 2312–2319.
77 T. J. McIntosh, *Biochim. Biophys. Acta - Biomembr.*, 1978, **513**, 43–58.
78 D. Quigley and P. M. Rodger, *J. Chem. Phys.*, 2008, **128**, 926.
79 M. Fitzner, G. C. Sosso, S. J. Cox and A. Michaelides, *Proc. Natl. Acad. Sci.*, 2019, **116**, 2009–2014.
80 J. Monroe, M. Barry, A. Destefano, P. A. Gokturk, S. Jiao, D. Robinson-Brown, T. Webber, E. J. Crumlin, S. Han and M. S. Shell, *Annu. Rev. Chem. Biomol. Eng.*, 2020, **11**, 523–557.

81 A. Alizadeh, M. Yamada, R. Li, W. Shang, S. Otta, S. Zhong, L. Ge, A. Dhinojwala, K. R. Conway, V. Bahadur, A. J. Vinciquerra, B. Stephens and M. L. Blohm, *Langmuir*, 2012, **28**, 3180–3186.
82 J. Chanda, L. Ionov, A. Kirillova and A. Synytska, *Soft Matter*, 2015, **11**, 9126–9134.